Nonlinear Effect of Dead Time in Small-Signal Modeling of Power-Electronic System Under Low-Load Conditions

Matias Berg, *Student Member, IEEE*, and Tomi Roinila, *Member, IEEE*

***Abstract*— Dead time is required to ensure that the switches of a synchronous switching inverter leg never conduct at the same time. During dead time, the current commutates to an antiparallel diode that can cause a voltage error depending on the instantaneous current direction. To measure a frequency response from a system, external injections are commonly required to perturb the system. The perturbation can change the current direction at the frequency of the injection, causing a voltage error at the injection frequency due to the dead time. The error depends on the perturbation amplitude, inductor current ripple, and fundamental current amplitude. This article proposes a describing-function method to model the dead-time effect under low-load conditions. It is shown that a nonlinear damping effect from the dead time can occur under low-load conditions and cannot be modeled with a resistor-like element. Real-time hardware-in-the-loop-simulation results are presented and used to demonstrate the effectiveness of the proposed method. Experimental measurements are used to verify the nonlinear dead-time effect.**

***Index Terms*— Dead time, describing function, frequency response, nonlinearity.**

I. Introduction

FREQUENCY-RESPONSE analysis is among the most widely used techniques in dynamic analysis and controller tuning of the power electronic systems. The basis of deriving the dynamic models lies in the linearity of the inspected system or linearizing the system around an operation point that yields a linear frequency response. Impedance-based stability is an application that is based on the measured or modeled frequency responses and has received a great deal of attention in the last few years [1]–[3].

A possible source of nonlinearity is the dead time that is required to prevent the shoot-through faults in the synchronous switching power converters. Dead time causes a voltage error that is dependent on the inductor current sign [4]. The inductor current sign can change due to an external disturbance that can be caused, for example, by a frequency-response measurement.

A typical frequency-response-measurement method of a power-electronics system is based on an external voltage/current injection that is placed, for example, on the top of the nominal input voltage or current or control signal. Fourier methods are then applied to extract the spectral information between the desired input and the output variables [5]. In a power-electronics system with the dead time, a measurement injection can change the current sign at the injected frequency and cause a voltage error that acts as a damping.

The dead-time effect regarding the small-signal dynamics has gained some attention in the literature. Several studies have modeled the dead-time effect with a resistor-like element [6]–[10]. Three-phase converters were analyzed in [6] and [7], and single-phase converters in [8] and [9]. In [10], the dead-time effect on the dynamics of a synchronous switching buck converter was analyzed, focusing on the charging of the drain–source capacitance during the dead time. The dead-time effect on the dynamics of a quasi-square-wave flyback converter was analyzed in [11].

The importance of the ripple effect is shown in [8], and a describing-function-based method is used to solve a resistor-like element to model the dead-time effect. The model predicts damping to occur when the fundamental current amplitude is higher than half of the peak-to-peak current ripple. Furthermore, it is assumed that the inductor current amplitude is the same as the injection current. This assumption in [8] is well grounded, because the output filter of the analyzed full-bridge inverter consists of only an inductor. However, if there was a resonance that increases the inductor current with respect to injection, this assumption would not be valid.

This article studies the dead-time effect under a low-load condition, where the inductor current fundamental component amplitude is lower than half the peak-to-peak ripple. In [8], the opposite assumption and operating point were used. Furthermore, in this article, the response in the inductor current that causes the dead-time effect is not considered small. Instead, we propose a describing-function-based method that models the output impedance as a function of injection amplitude and frequency. We show that resonance in the system can increase the inductor current so that a voltage error occurs or even saturates. Therefore, a moderate injection amplitude does not guarantee a linear operating region.

The remainder of this article is structured as follows. Section II examines the dead-time effect and the amplitude dependence in the frequency-response measurements. Section III derives a describing-function model for the error. The proposed amplitude-dependent output impedance is

Manuscript received September 27, 2019; revised December 9, 2019; accepted January 5, 2020. Date of publication January 17, 2020; date of current version November 5, 2020. This work was supported in part by the Fortum Foundation under Grant 201800119. Recommended for publication by Associate Editor Santanu Kapat. *(Corresponding author: Matias Berg.)*

The authors are with the Faculty of Information Technology and Communication Sciences, Tampere University, 33100 Tampere, Finland (e-mail: matias.berg@tuni.fi).

Color versions of one or more of the figures in this article are available online at http://ieeexplore.ieee.org.

Digital Object Identifier 10.1109/JESTPE.2020.2967341

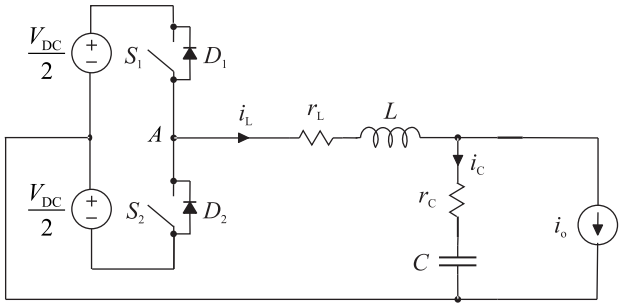

Fig. 1. Half-bridge inverter.

TABLE I
OPERATING POINT AND COMPONENT VALUES

Parameter	Value	Parameter	Value
V_{DC}	700 V	I_o	0-1.8 A
L	4 mH	r_L	10 mΩ
C	10 μF	r_C	10 mΩ
ω_s	2π60 rad/s	$V_{o,rms}$	120 V
f_s	10 kHz	T_{dead}	4 μs

introduced in Section IV. In Section V, hardware-in-the-loop (HIL) simulations and experimental measurements are used to verify the analyzed dead-time effect. Conclusions are drawn in Section VI.

II. Dead-Time Effect

This section begins by inspecting the voltage error that is caused by the dead time. We then analyze and model how the dead-time effect is visible in the frequency-response measurements and how the operating point and system parameters affect the dead-time effect. Throughout this article, it is assumed that the frequency-response measurement is performed with a sinesweep, where one frequency at a time is injected and measured.

A. Voltage Error Caused by Dead Time

Fig. 1 shows a half-bridge inverter that is used to analyze the dead-time effect. The switches and the diodes are analyzed with ideal components. However, in reality, the required dead time depends on the turn-off characteristics of the used semiconductor switches [12]. When the dead-time length is chosen, the changes in the switch characteristics with load current and temperature must be considered [13]. The dead time is not changed according to the operating conditions. In general, faster switching devices require shorter dead time than the lower switching devices. The operating point and the component values are given in Table I. A dead time value of 4 μs is applied in most parts of this article. This value (in a combination of the applied switching frequency of 10 kHz in the laboratory setup) was observed to demonstrate the nonlinear effect efficiently.

The dead time is used to delay the turn-on of switches S_1 and S_2, ensuring a period during which neither of the switches conducts. During dead time, the current commutates to either of diodes D_1 or D_2, depending on the instantaneous current sign [4]. Therefore, the dead time causes an instantaneous voltage error, v_{err}, in the inverter voltage during the dead time

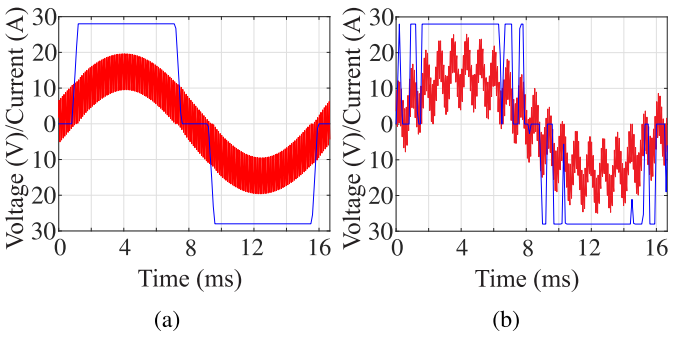

Fig. 2. Inductor current (red) and average voltage error (blue) waveforms when (a) fundamental current is higher than half the peak-to-peak current ripple and (b) with an added sinusoidal perturbation in the inductor current.

that can be given by

$$v_{err} = \text{sign}(i_L)V_{dc} \tag{1}$$

where V_{dc} and i_L are the dc voltage and the inductor current, respectively. In order to facilitate the analysis, the error is averaged over a switching cycle

$$v_{err}^{avg-Ts} = \frac{1}{T_s}\int_{\tau}^{\tau+T_s} v_{err}(t)dt \tag{2}$$

where T_s and T_{dead} are the switching cycle and the dead-time lengths, respectively. The resulting maximum average voltage error is

$$V_{err}^{max} = \left|v_{err}^{avg-Ts}\right| = \left|\text{sign}(i_L)\frac{T_{dead}}{T_s}V_{dc}\right| \tag{3}$$

which yields 28 V with the parameters of Table I. The fundamental component of a square wave with the amplitude of 28 V is $4/\pi$ 28 V = 35.56 V. The value of the average voltage error has been analyzed in the literature earlier [4], [12]

Fig. 2(a) shows the averaged voltage error over a 60-Hz fundamental cycle. The error has the same sign as the current. However, during the period of current zero crossings, the average voltage error is zero. In Fig. 2(b), a perturbation is added to the inductor current, and a voltage error appears at the perturbation frequency due to the changes in the current zero crossings. The zero-crossing period was modeled in [14], and a similar approach was used for modeling the dead-time effect in [9]. However, this article focuses on modeling the dead-time effect under a low-load condition, where the 60-Hz fundamental current component is lower than half the peak-to-peak inductor current ripple.

Fig. 3(a) and (b) shows the inductor current and the averaged voltage error under low-load conditions. In Fig. 3(a), there is no fundamental 60-Hz component in the inductor current, and in Fig. 3(b), the fundamental component is lower than half the peak-to-peak current ripple. The average voltage error during the whole fundamental cycle is zero, because the inductor current crosses zero during every switching cycle, and the instantaneous error has both signs during a switching cycle. Fig. 3(c) illustrates a case where a perturbation is added to the current fundamental component, and the sum has a higher amplitude than half the peak-to-peak current ripple. Therefore, a voltage error appears when there are no zero crossings within a switching cycle or a zero current clamping occurs.

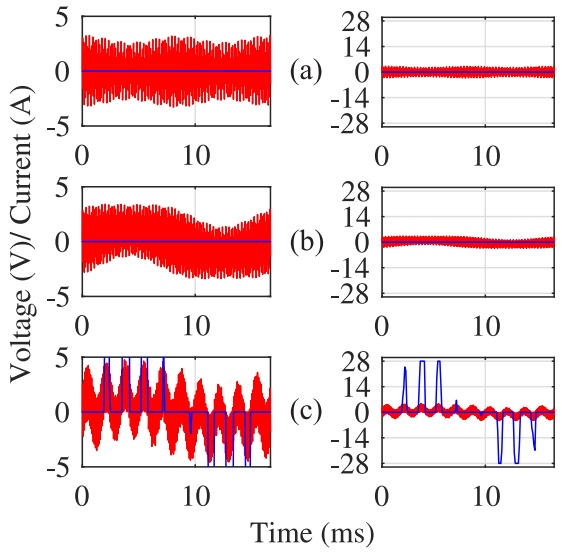

Fig. 3. Inductor current waveforms (red) and averaged voltage errors (blue) with different fundamental current amplitudes (a) 0, (b) 1, and (c) 1 A with a perturbation of 1.5 A at 600 Hz.

B. Perturbation Amplitude Dependence

The half-bridge inverter in Fig. 1 is simulated with MATLAB/Simulink. A current injection is made with the output current, i_{o}, to measure the output impedance, $Z_{\mathrm{o}} = \hat{v}_{\mathrm{o}}/\hat{i}_{\mathrm{o}}$. The fundamental load current, a 60-Hz component, A_{fund}, is provided by the current sink if required. In the following, the current sink draws no 60-Hz current component, and the current sink is used only for the injection. Fig. 4 shows the simulated measurement of the output impedance when no dead time is applied in the switching as the benchmark. The simulation is done two times with the injection amplitudes of 0.5 and 2 A.

A dynamic model of the system is created based on the parallel connection of the filter inductor impedance, Z_{L}, and filter capacitor impedance, Z_{C}

$$Z_{\mathrm{C}} = r_{\mathrm{C}} + \frac{1}{sC} \tag{4}$$

$$Z_{\mathrm{L}} = r_{\mathrm{L}} + sL \tag{5}$$

$$Z_{\mathrm{o}}(s) = \frac{Z_{\mathrm{C}} Z_{\mathrm{L}}}{Z_{\mathrm{C}} + Z_{\mathrm{L}}} = \frac{r_{\mathrm{C}} s^2 + \left(\frac{r_{\mathrm{L}} r_{\mathrm{C}}}{L} + \frac{1}{C}\right) s + \frac{r_{\mathrm{L}} r_{\mathrm{C}}}{CL}}{s^2 + \frac{r_{\mathrm{L}} + r_{\mathrm{C}}}{L} s + \frac{1}{CL}} \tag{6}$$

where L, C, r_L, and r_C denote the inductance, capacitance, inductor resistance, and capacitor resistance, respectively. As shown in Fig. 4, the model corresponds to the simulations according to the linear circuit theory.

Next, the output impedance simulation is repeated when a dead time of 4 μs is applied in the switch control signals. Fig. 5 compares the results with the linear model, $Z_{\mathrm{o}}(s)$. It is apparent from Fig. 5 that the dead time makes the system highly nonlinear, and the linear model cannot be used to model the system. With the injection amplitude of 0.5 and 1 A, the resonance is damped. On the other hand, with the injection amplitudes of 2 and 3 A, a damping appears at lower frequencies and the resonance is less damped.

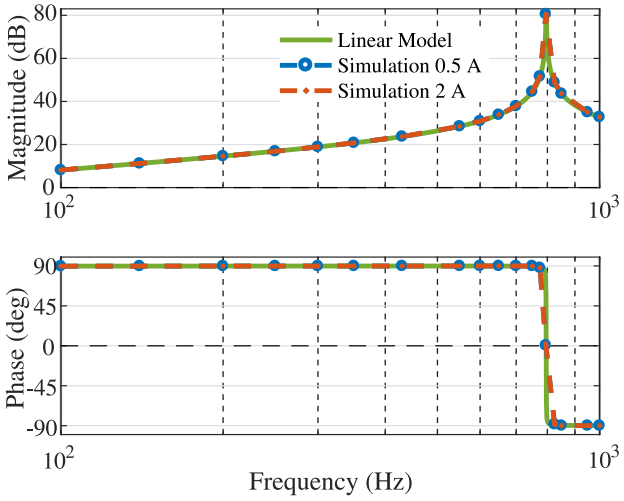

Fig. 4. Output impedance from a simulation without the dead time with different injection amplitudes.

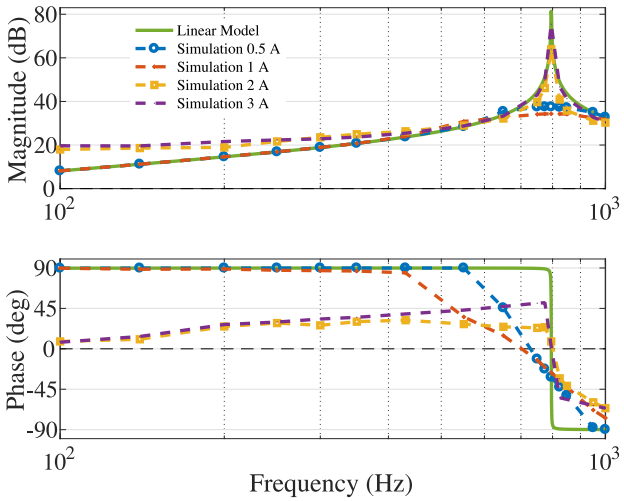

Fig. 5. Output impedance, Z_o, measured from a simulation with the dead time and different injection amplitudes.

Therefore, a resistor-like element that is constant at all frequencies cannot be used to model the dead-time effect.

It is known that the error caused by the dead time is dependent on the inductor current. Therefore, it is useful to look at the output current-to-inductor current dynamics. The transfer function can be given by

$$G_{\mathrm{oL}}(s) = \frac{Z_{\mathrm{C}}}{Z_{\mathrm{C}} + Z_{\mathrm{L}}} = \frac{\frac{r_{\mathrm{C}}}{L} s + \frac{1}{CL}}{s^2 + \frac{r_{\mathrm{L}} + r_{\mathrm{C}}}{L} s + \frac{1}{CL}}. \tag{7}$$

Fig. 6 compares the modeled and simulated $G_{\mathrm{oL}}(s)$. Similar to the case of the output impedance, the dead-time effect is visible and the linear model is not valid. Fig. 7 shows the absolute values of the inductor current and the voltage error with different injection amplitudes. It can be seen that the resonance amplifies the inductor current, which increases the voltage error. However, the voltage error has its maximum value $V_{\mathrm{err}}^{\max}$ according to (3). When the error saturates to the maximum value, its effect on the frequency response begins

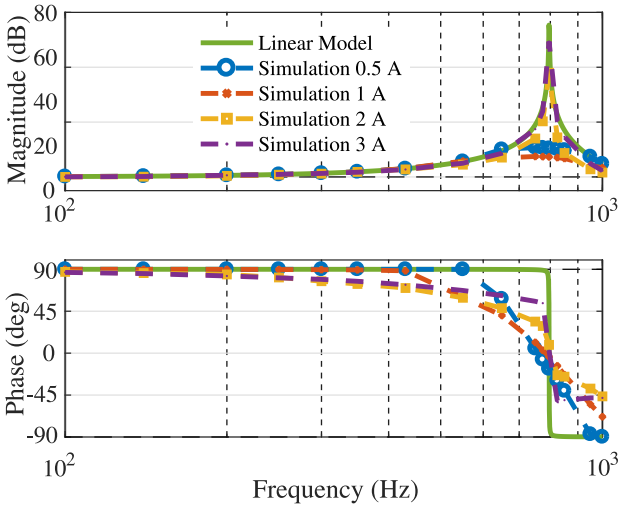

Fig. 6. Output current-to-inductor current transfer function, G_{oL}, measured from a simulation with different injection amplitudes.

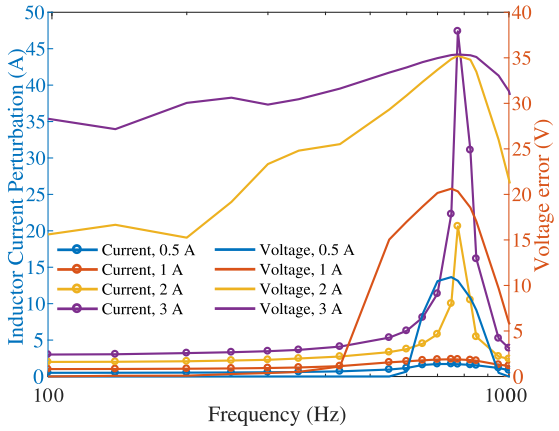

Fig. 7. Simulated absolute values of the inductor current and the voltage error with different injection amplitudes.

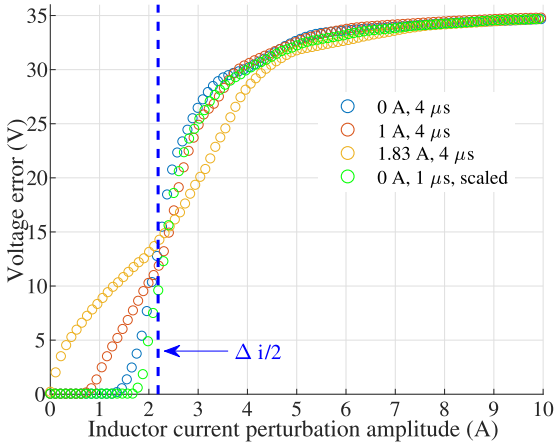

Fig. 8. Simulated voltage error as a function of the inductor current perturbation amplitude with different fundamental current amplitudes.

to diminish. It can be also noted that there is no voltage error at all if the inductor current amplitude is not high enough.

Fig. 8 illustrates how the error behaves as a function of the inductor current perturbation amplitude. For the simulations in Fig. 8, the filter capacitor was changed from 10 to 0.5 μF in order to reduce the reactive current fundamental component. All injections were made at 650 Hz. With zero fundamental current amplitude, there is a dead zone below which there is no voltage error. When the fundamental current amplitude is increased, the dead zone shortens until the fundamental amplitude is approximately half the peak-to-peak current ripple, $\Delta i/2$

$$\Delta i = \frac{V_{dc} T_s}{4L}. \tag{8}$$

Half the peak-to-peak ripple, $\Delta i/2$, is 2.19 A with the parameters of Table I.

Because the gain of $G_{oL}(s)$ is close to 0 dB at low frequencies, the injection amplitude must be higher than half the peak-to-peak ripple for the error to occur. This can be seen in Fig. 7. When the perturbation amplitude is high enough, the error saturates to the fundamental component of the square-wave voltage error. The saturation begins when the perturbation amplitude equals the sum of half the peak-to-peak current ripple and the fundamental current. After this point, the increase in the perturbation amplitude affects the whole fundamental cycle; this can be seen from Figs. 7 and 8. Between the dead zone and the saturation is a slope region that can be seen well from Fig. 8 in the case where the fundamental current amplitude is 1 A. This behavior of the voltage error under low-load conditions was illustrated in [9] but not analyzed.

Fig. 8 also shows the voltage error when the dead time is 1 μs. The error is scaled by multiplying it by 4 in order to have the maximum error, V_{err}^{max}, unchanged compared to the case with the dead time of 4 μs according to (3). By inspecting the error as a function of the current with $A_{fund} = 0$, Fig. 8 shows that there is a voltage error on the lower inductor current perturbations than $\Delta i/2$. This is partly due to the approximation of $\Delta i/2$ in (8) that gives the ripple when the duty cycle is 0.5 (that is, around the fundamental component zero crossing).

Furthermore, Fig. 8 reveals that the dead-time length not only affects the maximum voltage error, V_{err}^{max}. With $T_{dead} = 1$ μs, the error remains zero with higher inductor current-response amplitudes. This can be explained with a zero current clamping effect, which causes a voltage error. For a zero current clamping to occur, it is sufficient for the current to drop to zero during the dead time, and remain zero for the rest of the dead-time length. The maximum current change during the dead time is approximated by

$$i_{clamp}^{max} = \frac{V_{dc} T_{dead}}{2L}. \tag{9}$$

If the zero is crossed for i_{clamp}^{max} or fewer Amperes before the current slope direction changes, a zero current clamping occurs. The zero current clamping effect is the first source of voltage error rather than the main dead-time effect. The zero current clamping effect and the voltage error have been analyzed in [15].

III. Describing-Function Model

A describing-function model for the voltage error can be developed based on the observations from the voltage error

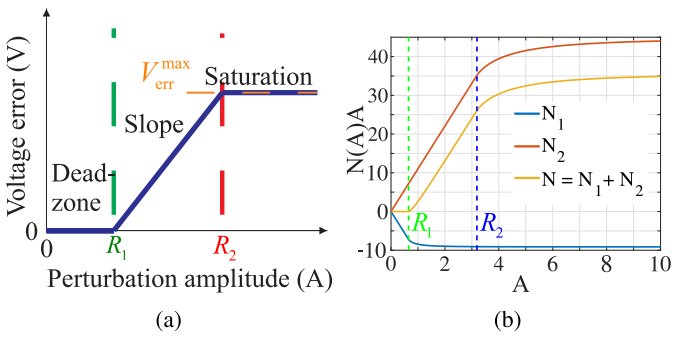

Fig. 9. (a) Dead zone, slope, and saturation that are modeled in frequency domain with (b) describing function.

as a function of the inductor current perturbation amplitude, current ripple, and current fundamental component in Fig. 8. Therefore, a describing-function model consisting of a dead zone, a slope, and a saturation illustrated in Fig. 9(a) must be created.

With lower current perturbation amplitudes, A, than R_1, there is no voltage error, and with higher than R_2, the error saturates. The zero current clamping effect reduces R_1 by $i_{\text{clamp}}^{\max}$ according to (9). R_1 and R_2 are defined by

$$R_1 = \frac{\Delta i}{2} - A_{\text{fund}} - i_{\text{clamp}}^{\max} \tag{10}$$

$$R_2 = \frac{\Delta i}{2} + A_{\text{fund}}\cos(\phi) \tag{11}$$

where A_{fund} is the fundamental current amplitude. The reactive current produced by the capacitor with amplitude A_{react} cannot be neglected, because it affects R_2 if the inductor current fundamental component is not in phase with the ripple. Therefore, the reactive current component has to be considered

$$A_{\text{react}} = V_o 2\pi 60C. \tag{12}$$

Therefore, the fundamental current amplitude is given by

$$A_{\text{fund}} = \sqrt{A_{\text{real}} + A_{\text{react}}}. \tag{13}$$

The angle ϕ in (11) is given by

$$\phi = \tan^{-1}\left(\frac{\text{A}_{\text{react}}}{\text{A}_{\text{real}}}\right) \tag{14}$$

where A_{real} is the 60-Hz component current drawn by the current sink. Between R_1 and R_2, the error increases from zero to $V_{\text{err}}^{\max}$ by the slope k

$$k = \frac{V_{\text{err}}^{\max}}{R_2 - R_1}. \tag{15}$$

Therefore, the error model, $N(A)$, can be created by summing the two describing-function models, $N(A)_1$ and $N(A)_2$, both modeling slope and saturation [16]

$$N(A)_1 = \frac{-2k}{\pi}\left[\sin^{-1}\left(\frac{R_1}{A}\right) + \frac{R_1}{A}\sqrt{1 - \left(\frac{R_1}{A}\right)^2}\right] \tag{16}$$

$$N(A)_2 = \frac{2k}{\pi}\left[\sin^{-1}\left(\frac{R_2}{A}\right) + \frac{R_2}{A}\sqrt{1 - \left(\frac{R_2}{A}\right)^2}\right] \tag{17}$$

$$N(A) = \Re[N(A)_1 + N(A)_2]. \tag{18}$$

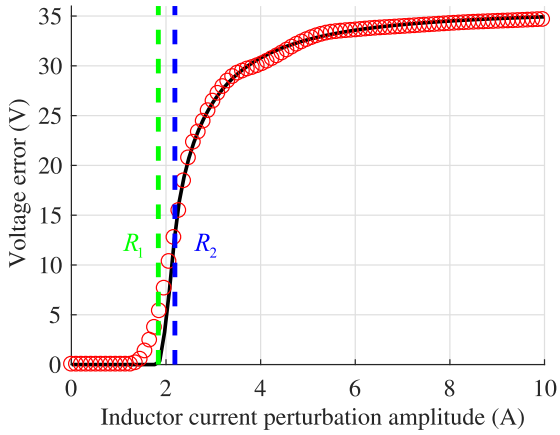

Fig. 10. Simulation (circles) and model (solid line) of the voltage error as a function of the inductor current perturbation amplitude with a fundamental current of 0 A.

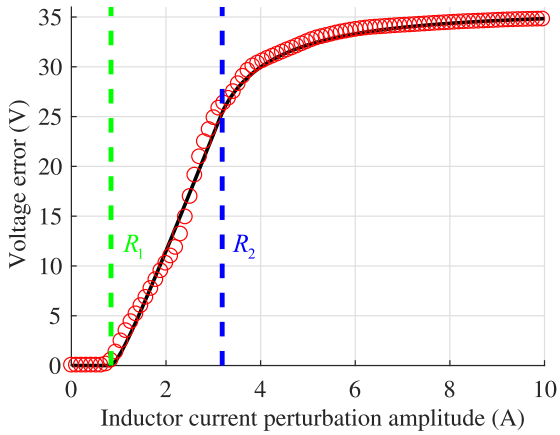

Fig. 11. Simulation (circles) and model (solid line) of the voltage error as a function of the inductor current perturbation amplitude with a fundamental current of 1 A.

Due to the dead zone, the sum of the slopes must be zero before R_1. Therefore, the slope of $N(A)_1$ is $-k$. Fig. 9(b) shows how $N(A)_1$ and $N(A)_2$ sum up to $N(A)$.

Figs. 10–12 compare the proposed model, $N(A)A$ as a function of A, with the simulated voltage error with the fundamental current amplitudes of 0, 1, and 1.83 A, respectively. The fundamental amplitude of 1.83 A was chosen in order to have R_1 in (10) zero. The proposed model estimates the nonlinear error sufficiently well. However, regardless of modeling, the zero current clamping effect the model for R_1 in Fig. 10 and the approximation with a single slope in Fig. 12 are not completely accurate.

IV. Amplitude and Frequency Response

This section deals with the output impedance that is affected by the nonlinear dead-time effect. Based on the describing-function model $N(A)$, an output impedance model that depends on both the injection amplitude and injection frequency is derived.

Due to the nonlinear voltage error, a transfer function must be defined as a function of the amplitude A and frequency ω. Therefore, the notation of the inductor and capacitor

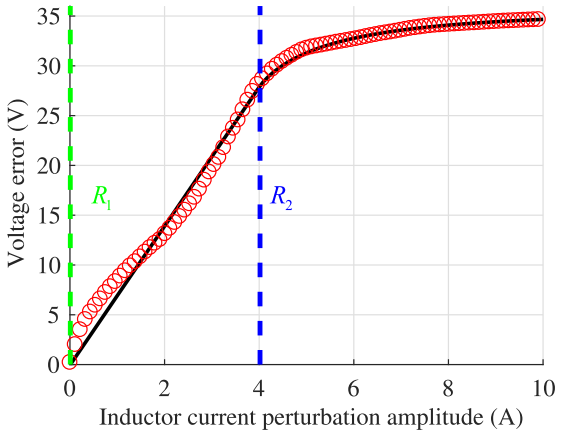

Fig. 12. Simulation (circles) and model (solid line) of the voltage error as a function of the inductor current perturbation amplitude with a fundamental current of 1.83 A.

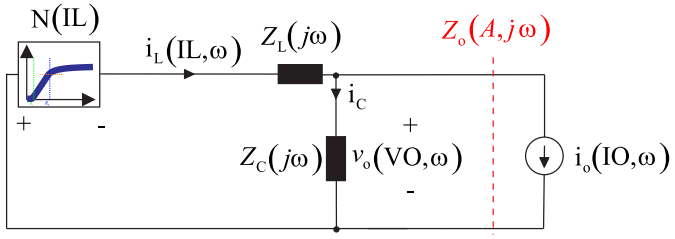

Fig. 13. Nonlinear frequency-domain circuit from where IL must be solved for every input combination of IO and ω.

impedance subsystems is changed from $Z_{\mathrm{L}}(s)$ and $Z_{\mathrm{C}}(s)$ to $Z_{\mathrm{L}}(j\omega)$ and $Z_{\mathrm{C}}(j\omega)$, respectively. The effect of $N(A)$ is included in the output impedance and, therefore, becomes a function of the input amplitude in addition to the frequency Therefore, the output impedance is expressed as $Z_{\mathrm{o}}(A, j\omega)$.

Fig. 13 shows a frequency-domain circuit presentation of the nonlinear system. The capacitor and inductor impedances are the traditional linear elements. However, the nonlinear voltage error is in series with the inductor impedance as a reverse-biased nonlinear current-dependent voltage source. The equation based on the circuit can be given by

$$|N(\mathrm{IL}) + Z_{\mathrm{L}}(j\omega) + Z_{\mathrm{C}}(j\omega)|i_{\mathrm{L}}(\mathrm{IL}, \omega) - |Z_{\mathrm{C}}(j\omega)|i_{\mathrm{o}}(\mathrm{IO}, \omega) = 0. \quad (19)$$

IO, VO, and IL are the phasors of the output current, output voltage, and inductor current, respectively. IL must be solved for each input combination on IO and ω. The phasors are analyzed separately at different frequencies, ω. $N(\mathrm{IL})$ is the analytical expression from (18). The equation can be solved, for example, by using the MATLAB *fzero* function. The solved $i_{\mathrm{L}}(\mathrm{IL}, \omega)$ is in a zero phase shift, because the equation could be solved only for the absolute value. Thus, the output current i_{o} must be resolved in order to find out the relational phase shift

$$i_{\mathrm{o}}(\mathrm{IO}, \omega) = \frac{[N(\mathrm{IL}) + Z_L(j\omega) + Z_C(j\omega)]i_L(\mathrm{IL}, \omega)}{Z_C(j\omega)}. \quad (20)$$

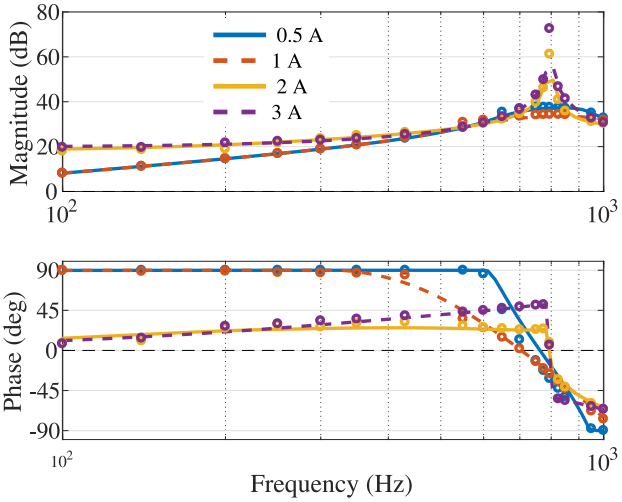

Fig. 14. Modeled (lines) and simulated (circles) output impedance with different perturbation amplitudes and a fundamental current of 0.64 A.

As the next step, the output impedance $Z_{\mathrm{o}}(A, j\omega)$ can be solved

$$Z_{\mathrm{o}}(A, j\omega) = -\frac{v_{\mathrm{o}}(\mathrm{VO}, \omega)}{i_{\mathrm{o}}(\mathrm{IO}, \omega)} = \frac{Z_{\mathrm{C}}(j\omega)i_{\mathrm{o}}(\mathrm{IO}, \omega) - Z_{\mathrm{C}}(j\omega)i_{\mathrm{L}}(\mathrm{IL}, \omega)}{i_{\mathrm{o}}(\mathrm{IO}, \omega)}. \quad (21)$$

Fig. 14 compares the modeled and the simulated output impedance, $Z_{\mathrm{o}}(A, j\omega)$. The model predicts well that, with low injection current amplitudes when the inductor current perturbation amplitude is small enough, the resonance is damped. On the other hand, the error saturates around the resonance with higher injection amplitudes and the undamped resonance becomes visible again. Higher injection amplitudes than R_1 cause errors at lower frequencies, which can be seen as damping.

Fig. 15 shows the modeled amplitudes of the voltage error and inductor current corresponding to the case of Fig. 14. As it can be seen, the error saturates at the resonance in the case of injection amplitudes of 2 and 3 A. Due to this, the damping effect is diminished as it can be seen from Fig. 14. Figs. 16 and 17 compare the model with the simulation when the fundamental load current is 1 A and the inductor current is 1.19 A. However, the effect is modeled only at the fundamental frequency of the square-wave-like voltage error.

V. HIL Simulation and Experimental Verification

This section deals with HIL simulations and experimental laboratory measurements. First, we take a look at the changes that are caused by dc capacitors of the used practical circuit. Second, a voltage injection is used to measure the output impedance in an HIL simulation. Third, a practical laboratory setup is used to verify the nonlinear dependence on the injection amplitude.

A. Practical Circuit

Fig. 18 shows the circuit diagram of the experimental setup. In the practical half-bridge inverter, there are dc capacitors,

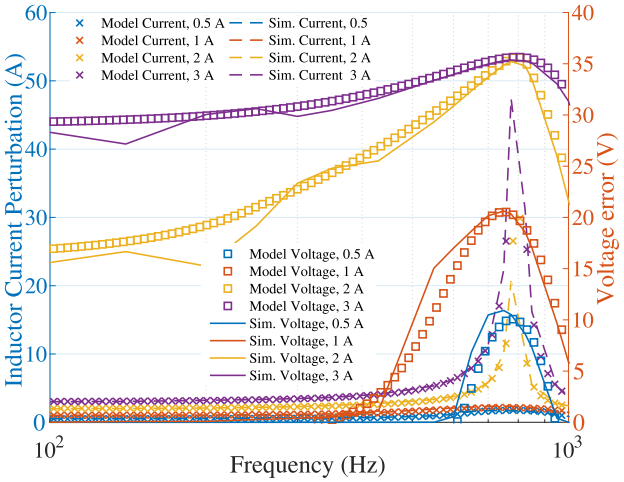

Fig. 15. Modeled and simulated inductor current amplitude and voltage error with different perturbation amplitudes and a fundamental current of 0.64 A.

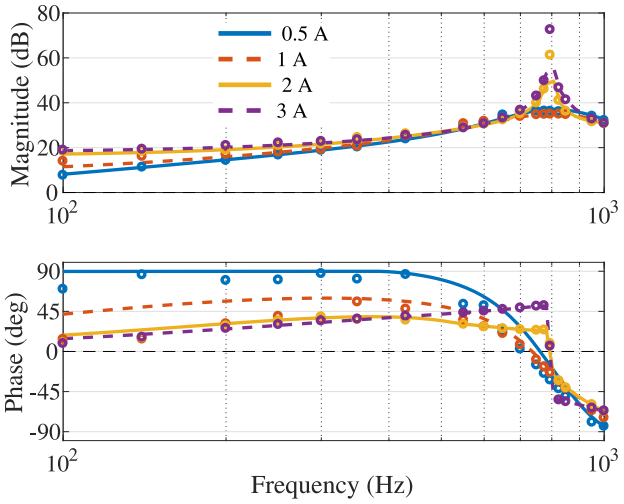

Fig. 16. Modeled (lines) and simulated (circles) output impedance with different perturbation amplitudes and a fundamental current of 1.19 A.

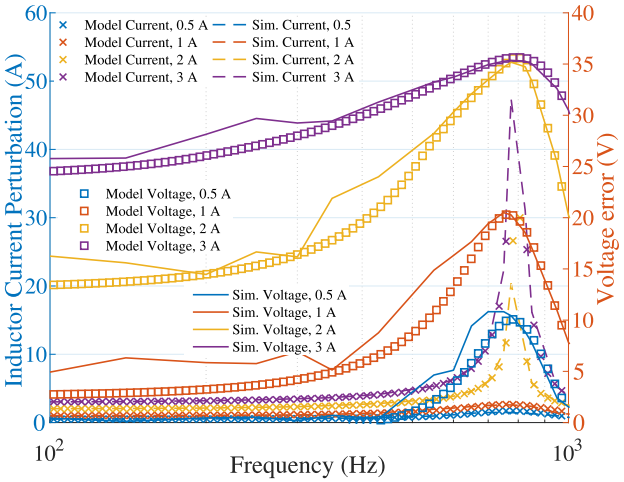

Fig. 17. Modeled and simulated inductor current amplitude and voltage error with different perturbation amplitudes and a fundamental current of 1.19 A.

C_{dc}, instead of the two ideal voltage sources that were used previously. Because the dc voltage source is a dynamic short circuit, a parallel connection of the dc capacitors, Z^{par}_{dc-C},

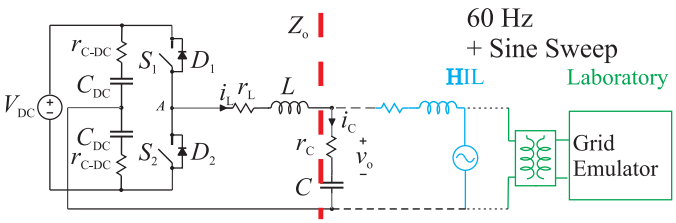

Fig. 18. Circuit diagram of the HIL simulations and laboratory experiment.

TABLE II
OPERATING POINT AND COMPONENT VALUES OF THE HIL SIMULATION

Parameter	Value	Parameter	Value
f_s	20 kHz	T_{dead}	2 μs
V_{DC}	700 V	$V_{o,rms}$	120 V
L	1.2mH	r_L	0.16Ω
C	9.8 μF	r_C	0.11 Ω
C_{DC}	500 μF	$r_{C\text{-}DC}$	0.246 Ω
ω_s	2π60 rad/s		

is visible in series with the inductor and is, therefore, included in the inductor impedance

$$Z_{C-dc}(j\omega) = r_{C-dc} + \frac{1}{j\omega C_{dc}} \tag{22}$$

$$Z^{par}_{C-dc} = \frac{Z_{C-dc} Z_{C-dc}}{Z_{C-dc} + Z_{C-dc}} \tag{23}$$

$$Z_L(j\omega) = Z^{par}_{C-dc} + r_L + j\omega L \tag{24}$$

where r_{C-dc} is the equivalent series resistance of the dc capacitor.

The analysis focuses on the antiresonance in (24), because with the used laboratory equipment, it was not possible to inject the voltages that cause high enough current at the *LC* parallel resonant frequency to demonstrate the saturation effect.

For the sake of simplicity, the filter capacitor is not included in the output impedance. Therefore, the nonlinear circuit equation that must be solved for IL reduces to

$$|\mathrm{N(IL)} + Z_L(j\omega)|i_L(\mathrm{IL}, \omega) + v_o(\mathrm{VO}, \omega) = 0. \tag{25}$$

The output impedance can be solved from

$$Z_o(A, j\omega) = -\frac{v_o(\mathrm{VO}, \omega)}{i_L(\mathrm{IL}, \omega)}. \tag{26}$$

The parameters of the HIL simulation in this section are given in Table II.

B. HIL Simulations

The circuit of Fig. 18 is simulated with Typhoon HIL model 402. The phase-locked loop (PLL) is omitted for simplicity. The inductor current amplitude, I_L, and the capacitor current amplitude, I_C, are 1.01 and 0.64 A, respectively. The 60-Hz fundamental voltage component is provided by the ideal voltage source that has a very small series-connected inductor and resistor to improve the simulation stability. The voltage source is also used to inject a sine sweep for the measurement. In order to demonstrate the nonlinear damping effect, high injection amplitudes are required.

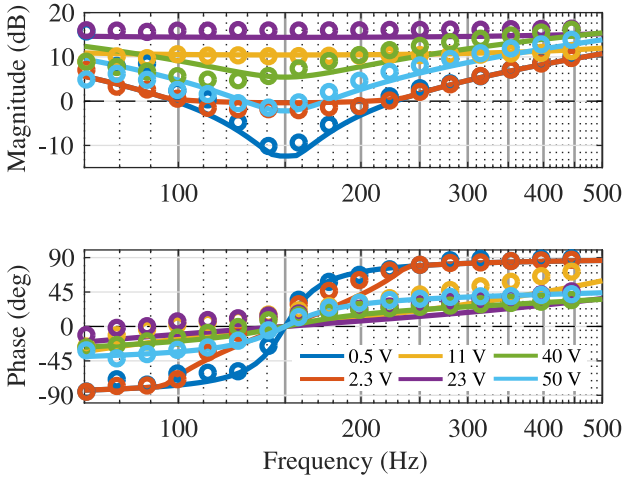

Fig. 19. HIL simulation (circles) and model (lines) of the open-loop output impedance of the grid-connected converter with different injection voltages.

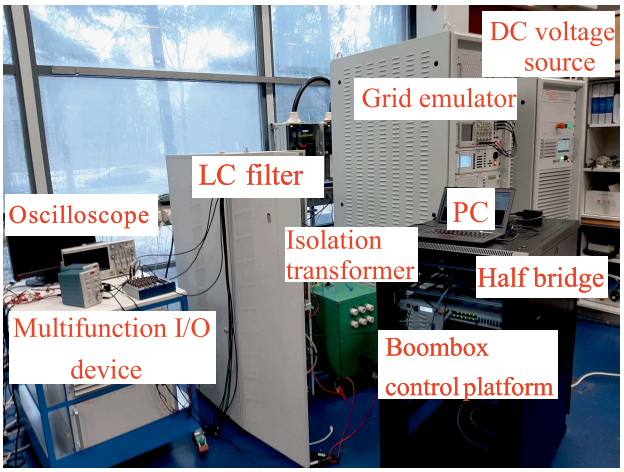

Fig. 20. Laboratory setup.

Fig. 19 shows the real-time HIL-simulated frequency response and the model around the antiresonance at 150 Hz. It can be seen that the model clearly predicts the damping as the function of the perturbation amplitude. The most striking result from Fig. 19 is that the damping increases when the injection amplitude is increased from 0.5 to 23 V. With injection amplitudes of 40 and 50 V, there is less damping, which is predicted correctly by the model. A notable change in the damping can be seen even with the injection amplitudes 0.5, 2.3, and 11 V, which are less than 10% of the fundamental 170-V component amplitude.

C. Laboratory Measurements and Comparison to Simulations

The nonlinear damping by the dead time is verified by laboratory measurements. Fig. 20 shows the laboratory setup for the circuit in Fig. 18. A low-bandwidth PLL is used to synchronize the half-bridge converter to the 60-Hz voltage provided by the grid emulator. The frequency response of the output impedance is measured by injecting a sine sweep with

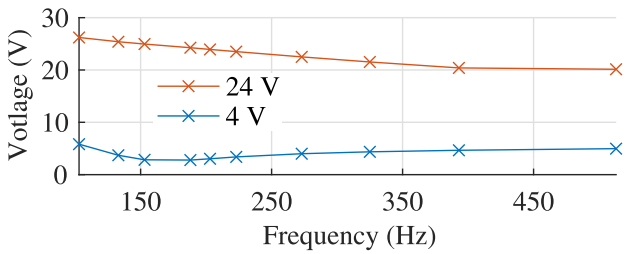

Fig. 21. Injected output voltage amplitude at different frequencies.

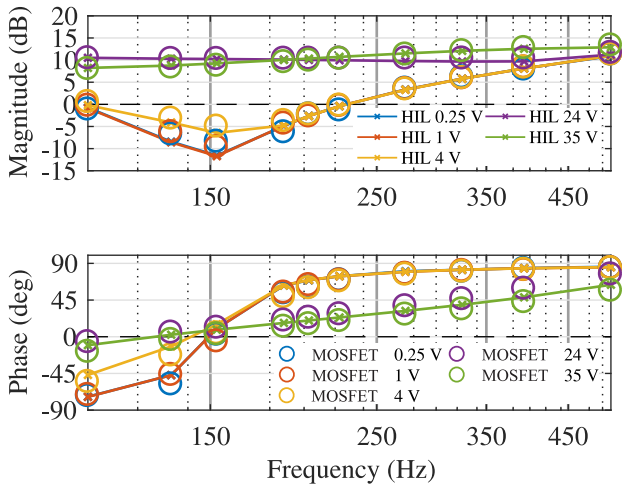

Fig. 22. Laboratory measurement of the open-loop output impedance of the grid-connected converter with MOSFETs with different injection voltages and HIL replication of the measurement.

a grid emulator. The measurements are performed separately with MOSFETs and insulated-gate bipolar transistors (IGBTs) in order to see the effect of nonideal switches. The used switch modules were the PEB Sic 8024 module and PEB 8032 module by Imperix.

Due to the used isolation transformer, there is a voltage drop in the value, which depends on the injected frequency, and the injected voltage over the capacitor is not the voltage over the grid emulator. Fig. 21 shows two injections as an example. The injected output voltage amplitude is not constant, and the injected voltage over the filter capacitor varies slightly between the IGBT and MOSFET measurements. The nominal values for the injections, 4 and 24 V, are chosen from the values at around 270 Hz. As it has been shown, the nonlinear dead-time effect is very amplitude-sensitive. Therefore, the practical measurement is replicated in an HIL simulation by injecting a voltage that in reality was over the filter capacitor.

Figs. 22 and 23 show the measured laboratory measurements with MOSFETs and IGBTs compared with the HIL simulations, respectively. The laboratory setup is shown in Fig. 20, and the passive component parameters of the setup are given in Table III. As stated earlier, ideal switches with ideal diodes were used in the HIL simulations.

The HIL simulation gives a result that corresponds to the laboratory measurements in the case of the MOSFETs, as shown in Fig. 22. Fig. 23 shows the converter output impedance with the IGBT. As shown in Fig. 23, there is a

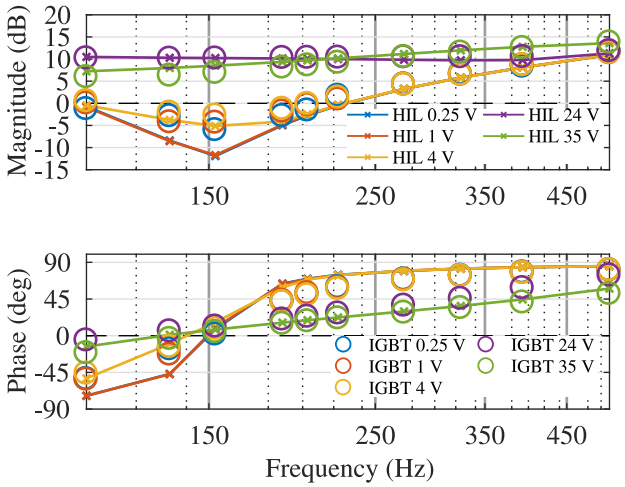

Fig. 23. Laboratory measurement of the open-loop output impedance of the grid-connected converter with IGBTs with different injection voltages and HIL replication of the measurement.

TABLE III
SYSTEM PARAMETER VALUES OF THE LABORATORY MEASUREMENTS

Parameter	Value	Parameter	Value
f_s	10 kHz	T_{dead}	4 μs
V_{DC}	700 V	$V_{o,rms}$	120 V
L	1.2mH	r_L	0.13Ω
C	10 μF	r_C	0.1 Ω
C_{DC}	500 μF	$r_{C\text{-}DC}$	0.246 Ω
ω_s	2π60 rad/s		

more visible difference in damping between the simulation in laboratory measurement with low injection amplitudes compared with the case with the MOSFET. This implies that nonidealities with the IGBT cause more problems regarding the modeling of the dead-time effect. On the other hand, the used dead time of 4 μs is not relevant for the MOSFETs, because it is unnecessarily long. However, the purpose of this article is to study the damping that stems from the dead time. With the two highest injection amplitudes, the HIL simulation matches accurately to the laboratory measurements. Furthermore, with the highest injection amplitude, the damping decreases below the resonance frequency that is visible in both the laboratory measurements and the HIL simulation. The nonidealities with MOSFETs could become more visible with higher switching frequencies.

VI. CONCLUSION

This article has investigated the nonlinear damping caused by the dead time effect under load conditions where the fundamental current component is less than half the peak-to-peak current ripple. The findings indicate that error caused by the dead time can be modeled with a dead zone, slope, and saturation as a function of the inductor current amplitude. Due to the dead zone, the effect cannot be modeled with a resistor-like element, as was used earlier in the literature with the dead time under different load conditions.

By using a describing function, we found a model for the error caused by the dead time under a low-load condition. The describing-function model in combination with linear circuit impedances was used to derive the output impedance of an inverter as a function of the injection amplitude. We observed that, even with a moderate measurement injection amplitude, a system resonance can increase the inductor current amplitude, making the nonlinearities become visible. This can occur especially in simulations, where ideal current source that can provide infinite voltage is used for the measurement injection. The proposed model works accurately with real-time HIL simulations that are becoming increasingly popular. Experimental measurements were provided for verifying the HIL simulations and the nonlinear dead-time effect.

This article represents the first occasion that the output impedance of a power electronic converter has been given as a function of the injection amplitude in addition to the injection frequency. Our article has some limitations regarding the nonidealities in practical semiconductor switches. In addition, low-order harmonics except the first one were assumed nonexistent. For example, considerable harmonics produced by a nonlinear load could change the effect. Nevertheless, we believe our article gives new theoretical background on the analysis of the nonlinear small-signal dead-time effect under low-load conditions. On a wider level, research is also needed to determine how the nonlinear dead-time effect and the measurement result behave under broadband injections that are becoming increasingly popular [5], [17].

REFERENCES

[1] B. Wen, R. Burgos, D. Boroyevich, P. Mattavelli, and Z. Shen, "AC stability analysis and *dq* frame impedance specifications in power-electronics-based distributed power systems," *IEEE J. Emerg. Sel. Topics Power Electron.*, vol. 5, no. 4, pp. 1455–1465, Dec. 2017.

[2] A. Aapro, T. Messo, T. Roinila, and T. Suntio, "Effect of active damping on output impedance of three-phase grid-connected converter," *IEEE Trans. Ind. Electron.*, vol. 64, no. 9, pp. 7532–7541, Sep. 2017.

[3] T. Roinila, T. Messo, and E. Santi, "MIMO-identification techniques for rapid impedance-based stability assessment of three-phase systems in DQ domain," *IEEE Trans. Power Electron.*, vol. 33, no. 5, pp. 4015–4022, May 2018.

[4] S.-G. Jeong and M.-H. Park, "The analysis and compensation of dead-time effects in PWM inverters," *IEEE Trans. Ind. Electron.*, vol. 38, no. 2, pp. 108–114, Apr. 1991.

[5] R. Luhtala, H. Alenius, T. Messo, and T. Roinila, "Online frequency response measurements of grid-connected systems in presence of grid harmonics and unbalance," *IEEE Trans. Power Electron.*, vol. 35, no. 4, pp. 3343–3347, Apr. 2020.

[6] S. Ahmed, Z. Shen, P. Mattavelli, D. Boroyevich, and K. J. Karimi, "Small-signal model of voltage source inverter (VSI) and voltage source converter (VSC) considering the DeadTime effect and space vector modulation types," *IEEE Trans. Power Electron.*, vol. 32, no. 6, pp. 4145–4156, Jun. 2017.

[7] A. Rodriguez-Cabero, M. Prodanovic, and J. Roldan-Perez, "Analysis of dynamic properties of VSCs connected to weak grids including the effects of dead time and time delays," *IEEE Trans. Sustain. Energy*, vol. 10, no. 3, pp. 1066–1075, Jul. 2019.

[8] M. Zhang, D. Yang, and X. Wang, "Accurate open-loop impedance model of single-phase voltage source inverter (VSI) considering the dead-time effects," in *Proc. 20th Workshop Control Modeling Power Electron. (COMPEL)*, Jun. 2019, pp. 1–5.

[9] M. Berg, T. Messo, T. Roinila, and P. Mattavelli, "Deadtime impact on the small-signal output impedance of single-phase power electronic converters," in *Proc. 20th Workshop Control Modeling Power Electron. (COMPEL)*, Jun. 2019, pp. 1–8.

[10] W. Qiu, S. Mercer, Z. Liang, and G. Miller, "Driver deadtime control and its impact on system stability of synchronous buck voltage regulator," *IEEE Trans. Power Electron.*, vol. 23, no. 1, pp. 163–171, Jan. 2008.

[11] Z. Zhang, S. Tian, and K. D. T. Ngo, "Small-signal equivalent circuit model of quasi-square-wave flyback converter," *IEEE Trans. Power Electron.*, vol. 32, no. 8, pp. 5885–5888, Aug. 2017.
[12] A. Mora, J. Juliet, A. Santander, and P. Lezana, "Dead-time and semiconductor voltage drop compensation for cascaded H-bridge converters," *IEEE Trans. Ind. Electron.*, vol. 63, no. 12, pp. 7833–7842, Dec. 2016.
[13] R. L. Bonkowski, "A technique for increasing power transistor switching frequency," *IEEE Trans. Ind. Appl.*, vol. IA-22, no. 2, pp. 240–243, Mar. 1986.
[14] G. Grandi, J. Loncarski, and R. Seebacher, "Effects of current ripple on dead-time distortion in three-phase voltage source inverters," in *Proc. IEEE Int. Energy Conf. Exhibit. (ENERGYCON)*, Sep. 2012, pp. 207–212.
[15] A. Rothstein and V. Staudt, "Detailed analysis of converter-output-voltage errors under light-load conditions," in *Proc. Int. Conf. Optim. Electr. Electron. Equip. (OPTIM), Int. Aegean Conf. Electr. Mach. Power Electron. (ACEMP)*, May 2017, pp. 336–341.
[16] J. T. Machadoa, A. M. Lopesa, D. Valerio, and A. M. Galhano, *Solved Problems in Dynamical Systems and Control*. Edison, NJ, USA: IET, 2016.
[17] T. Roinila, M. Vilkko, and J. Sun, "Online grid impedance measurement using discrete-interval binary sequence injection," *IEEE J. Emerg. Sel. Topics Power Electron.*, vol. 2, no. 4, pp. 985–993, Dec. 2014.

Matias Berg (Student Member, IEEE) received the B.Sc. (Tech.) and M.Sc. (Tech.) degrees in electrical engineering from the Tampere University of Technology, Tampere, Finland, in 2015 and 2017, respectively. He is currently pursuing the doctoral degree with Tampere University, Tampere.

His research interest includes dynamic modeling of grid-following and grid-forming converters.

Tomi Roinila (Member, IEEE) received the M.Sc. (Tech.) and Dr.Tech. degrees in automation and control engineering from the Tampere University of Technology (TUT), Tampere, Finland, in 2006 and 2010, respectively.

He is currently an Academic Researcher with Tampere University. His main research interests include modeling and control of grid-connected power-electronics systems and modeling of multiconverter systems.